Microstructure and Mechanical Properties of a Ni-Based Superalloy Thin Film Investigated by Micropillar Compression

Y. KALCHEV, R. ZEHL, T. PIOTROWIAK, A. KOSTKA, D. NAUJOKS, J. PFETZING-MICKLICH, and A. LUDWIG

The microstructure and local micromechanical properties of a Ni-based superalloy thin film produced by magnetron sputtering using ERBO/1 sputter targets were investigated. The thin film consists of columnar nanograins (an average size of ~ 45 nm) with mostly < 111 > orientation. Inside the nanograins, very fine nanotwins with an average thickness of ~ 3 nm are present. In-situ micropillar compression tests, complemented by nanoindentation, were conducted to evaluate the mechanical characteristics. The microhardness and Young's modulus of the thin film correspond to ~ 11 and 255 GPa, respectively, the critical strength to ~ 4 GPa. The plastic deformation of the micropillars occurs through the formation of a shear band initiating at the top of the pillar. Inside the shear band, globular grains with random orientation form during the deformation process, while the regions near to the shear band remained unaffected.

I. INTRODUCTION

WHILE silicon (Si) is the material of choice for most microelectromechanical systems (MEMS), also new materials, which could withstand extreme conditions and higher stresses, are necessary. Although Si exhibits good mechanical properties at room temperature, its brittleness is restrictive.[1,2] Metallic materials are typically superior to ceramics or semiconductors as Si when it comes to fracture toughness and ductility.[3] The most established process to produce metallic MEMS structures is the LIGA process.[4] However, the LIGA process is, for the most part, limited to elementary Ni.[5] However, bulk Ni alloys proved to be way superior in terms of mechanical properties and chemical stability compared to pure elementary Ni.[6] Therefore, metallic alloys such as Ni-based superalloys could also be promising candidates for the next generation of MEMS devices for harsh environments.[1,2,7] Thin films for MEMS can be microstructured, e.g., by photolithographic lift-off processing.[8,9]

Ni-based superalloys have been widely applied in aerospace and energy generation as turbine blades and discs which operate under harsh conditions.[10–13] They exhibit exceptional creep strength and high-temperature corrosion resistance, which result in longer service time for structural components.[13–15] However, Ni-based superalloy thin films have been only rarely studied as possible candidate MEMS materials,[5] i.e., fabricated aluminized Ni-LIGA structures and observed superior tensile strength to pure Ni-LIGA structures.

Therefore, in this study, we focus our attention on the local mechanical properties of Ni-based superalloy thin films and compare them to published data. A prominent method to characterize Young's modulus and hardness of thin films is nanoindentation. However, nanoindentation lacks direct information of the stress–strain evolution. Instead, micromechanical testing, such as compression of micropillars, can provide the stress–strain data, which complements conventional nanoindentation.

In the present study, a Ni-based superalloy thin film with ~ 2.5 μm thickness was sputtered at 500 °C onto a single crystal sapphire wafer. X-ray diffraction (XRD), scanning electron microscopy (SEM), and transmission

Y. KALCHEV is with the Chair for Materials Science and Engineering, Ruhr-University Bochum, Bochum, Germany. R. ZEHL and T. PIOTROWIAK are with the Chair of Materials Discovery and Interfaces, Ruhr-University Bochum, Bochum. A. KOSTKA, D. NAUJOKS and J. PFETZING-MICKLICH are with the Center for Interface-Dominated High Performance Materials (ZGH), Ruhr-University Bochum, Bochum. Contact e-mail: Janine.Pfetzing@ruhr-uni-bochum.de A. LUDWIG is with the Chair of Materials Discovery and Interfaces, Ruhr-University Bochum, Bochum and also with the Center for Interface-Dominated High Performance Materials (ZGH), Ruhr-University Bochum, Bochum.

electron microscopy (TEM) were used to study its crystalline phases and microstructure. Nanoindentation and *in-situ* micropillar compression tests were performed in a SEM to investigate the mechanical properties of the superalloy thin film. After deformation, the microstructural changes were observed using post-mortem TEM. Deformation mechanisms of the nanograined superalloy thin film were identified and discussed.

II. EXPERIMENTAL METHODS

A. *Material Processing*

The superalloy thin film sample was synthesized in a commercial multi-cathode magnetron co-sputter chamber (ATC 2200, AJA International, Inc.). Alloy targets of the Ni-based superalloy ERBO/1 (for chemical composition see Table I) were mounted on two opposing cathodes confocally aligned with a tilt angle of 27° with respect to the cathode's axis of symmetry. As substrate, a sapphire wafer heated to 500 °C (c-plane orientation < 0001 >, 100 mm × 650 μm, single side polished, by Situs Technicals GmbH) was used. The deposition was done with Ar as process gas at a constant flux of 50 sccm, a pressure of 0.5 Pa at 500 °C. The chamber's base pressure was 0.011 Pa. Both ERBO/1 targets were sputtered using high-power impulse magnetron sputtering (HiPIMS) power supply in unipolar mode at approximately 900 V, 0.22 A, and a frequency of 100 Hz with a pulse length of 40 μs (0.4 pct duty cycle) for 13,000 s. A peak current density of 1.6 A cm^{-2} was yielded with a peak current of 130 A and was normalized with respect to a target area of about 78.54 cm^2. For the used sputter parameters, a deposition rate of 0.156 nm s^{-1} was determined. A film thickness of 2.5 μm was reached after a deposition time of 13,000 s.

ADL power supplies of type GX 60/1000 (6 kW 1000 V Dual) were used in combination with a pulse power controller SIPP2000USB-Dual and HiPIMS measurement system MY2015-MY2019 from MELEC GmbH, controlled by MCC (v.2.3.x) measurement software. HiPIMS was used to improve film adhesion, to increase the film density and to decrease surface roughness. During HiPIMS, a large fraction of the sputtered target atoms are being ionized.[16–20] To further accelerate these ions, a substrate bias was used (200 V, 38 W forward power, 3 W reflected power) during the sputter process.

B. *Microstructure, Chemical Composition, and Phase Formation*

For alloy characterization, a small piece (50 × 50) mm^2 was cut out of the wafer using a Disco Dicing Saw DAD3220 with VT07-SD320-VC100-75 cutting discs.

To identify the present phases in the 2-μm-thick film, X-ray diffraction (XRD) was carried out at room temperature (RT) on a Bruker D8 Discover X-ray diffractometer in Bragg–Brentano geometry using a 2D detector (VANTEC-500). The XRD system is equipped with an Incoatec IμS Cu high-brilliance microfocus X-ray source with λ = 0.15418 nm CuK$_\alpha$ radiation, operated at 1 mA tube current and 50 kV acceleration voltage. A collimator with a focus spot size of 1 × 1 mm was used, resulting in a 1 mm^2 measurement area on the sample. The sample was measured in coupled 2θ–θ configuration. In four consecutive steps, frames were taken at the $2\theta/\theta$ positions 30°/15°, 50°/25°, 70°/35°, and 90°/45° with a measurement time of 60 s, respectively. Hereby, the angle of the approached position depicts the center position of the detector. One frame collects the diffraction data in an angular 2θ range of approximately $\pm$ 20° around the center point, *i.e.*, from 30° to 70° for 50° 2θ. All frames were subsequently merged into one elongated frame and integrated with a slice cursor in the 2θ range from 19° to 107°, using the software DIFFRAC.SUITE EVA.

The chemical compositions and the microstructure of the thin film were investigated using a high-performance scanning electron microscope JEOL JSM-7200F, operating at an accelerating voltage of 10 or 20 kV, equipped with AZtecEnergy X-MaxN 80 mm^2 –EDX detector and AZtec analytical software. Secondary electron (SE) and Backscatter electron (BSE) micrographs with a resolution of 2048 × 1887 pixels were obtained and analyzed to determine the thin film microstructure. The EDX analyses were conducted at an accelerating voltage of 20 kV, at the input rate of 85,000 counts per second (cps), to verify the chemical composition of the superalloy thin film.

For high-resolution analysis of the microstructural features, cross-sectional TEM lamellae were prepared using focus a FEI Helios G4 CX ion beam (FIB) system operated at 30 kV. In the final thinning step 5 kV energy beam was applied for 2 min for each side of the lamella to minimize the beam damage. Subsequent TEM investigations were performed before and after the micromechanical testing using a JEOL JEM-ARM 200F

Table I. Chemical Compositions of the Bulk ERBO/1—Refs. [10, 14] Compared to the Superalloy Thin Film

	Ni	Co	Cr	W	Re	Al	Ti	Ta	Mo	Hf
ERBO/1 Bulk Alloy	63.0	10.0	7.5	2.1	1.0	12.6	1.3	2.2	(0.4)	(0.03)
Superalloy Thin Film	63.5	10.5	8.7	2.3	1.0	10.4	1.4	1.9	(0.3)	(0.03)

SEM EDX results are listed for the thin film. All values presented in this table are in at. percent.

aberration-corrected instrument operated at 200 kV to identify deformation mechanisms. TEM orientation imaging was performed using Nanomegas DigiSTAR system with a spot size of 1 nm, an area size of 300 × 300 nm, and a step size of 1.3 nm.

C. Mechanical Testing

Nanoindentation experiments with a maximum indentation depth of 100 nm were conducted at RT in an as-deposited superalloy thin film sample using an *in-situ* Nanomechanics/KLA InSEM HT nanoindenter. It was equipped with a diamond Berkovich tip, calibrated on fused silica. A standard continuous stiffness measurement (CSM) method was used and average modulus and average hardness were calculated using the Oliver–Pharr[21,22] method, for displacements between 30 and 100 nm. Additionally, to determine a critical yield stress for the superalloy thin film, cylindrical micropillars were micromachined *via* focused ion beam (FIB) using a FEI Helios G4 CX, with 30 kV acceleration voltage of the Ga ions. First, an area without any surface artifacts was selected. Then, the simultaneous rough milling of a batch of 9 trenches with an outer diameter of 20 μm, an inner diameter of 5 μm, and a depth of 2 μm was initiated, using a 2.9 nA current. Finally, the fine milling of the micropillars with outer and inner diameter of 5 and 1.3 μm, respectively, was conducted, using a 0.49 pA current. Figure 1(a) shows an array of nine micropillars micromachined with the longitudinal pillar axis perpendicular to the film surface of the superalloy thin film. It should be noted that the whole micropillar is located in the thin film, thus substantially decreasing the effect of the substrate on the values of the measured mechanical properties, which was revealed by TEM investigations of a compressed pillar, on comparing Figure 6(a). The micropillars exhibit roughly a height of ~ 2 μm and a diameter of ~ 1.25 μm, although the targeted height-to-width ratio was initially 2:1 (see Figure 1(b)). Compression testing of these micropillars was carried out *in-situ* in a SEM (Quanta 650 FEI ESEM) equipped with a nanomechanical testing system (ASMEC UNAT-SEM 2), described in detail in References 23, 24. The indenter was equipped with a flat punch diamond tip ($r = 10$ μm) and tests were conducted using a load/unload method with a constant displacement rate of 10 nm/s.

III. RESULTS

A. As-Deposited Microstructure, Composition, and Crystal Structure

Results of the EDX measurements on the superalloy thin film are shown in Table I (in at. percent) and compared to the nominal chemical composition of the ERBO/1 alloy,[10,14] which was used as a sputter target in this work (see Sect. II—A), with those from the thin film. The results show that the chemical composition of the thin film is very similar to the ERBO/1 bulk alloy. With respect to the measurement uncertainty of EDX analyses (about 1 at. pct), the chemical contents of all elements in the thin film are almost identical to that of the bulk alloy, except for Cr (+ 1.2 pct) and Al (− 2.2 pct).

Figure 2 shows the results of the XRD measurement: The diffraction pattern exhibits two pronounced peaks (see Figure 2), which are typical for a *Fm-3m* FCC single-phase crystallographic structure with $a = 0.351$ nm.[25,26] The two present peaks indicate that the thin film is strongly textured, with preferred < 111 > and < 222 > crystallographic orientations (see Figure 2). The < 111 > crystallographic orientation is typical for FCC metals and has been reported in several previous studies.[5,7,27] The XRD results show the presence of a single phase γ (FCC) in the thin film, without any secondary phases being detected.

To characterize the as-deposited microstructure of the superalloy thin film, SEM and TEM investigations were carried out (Figure 3). The SEM images of the thin film surface show a very fine, nanograined microstructure, shown in Figures 3(a) through (b). The cross-sectional TEM images (see Figures 3(c) through (d)) show columnar nanograins, with a growth direction parallel
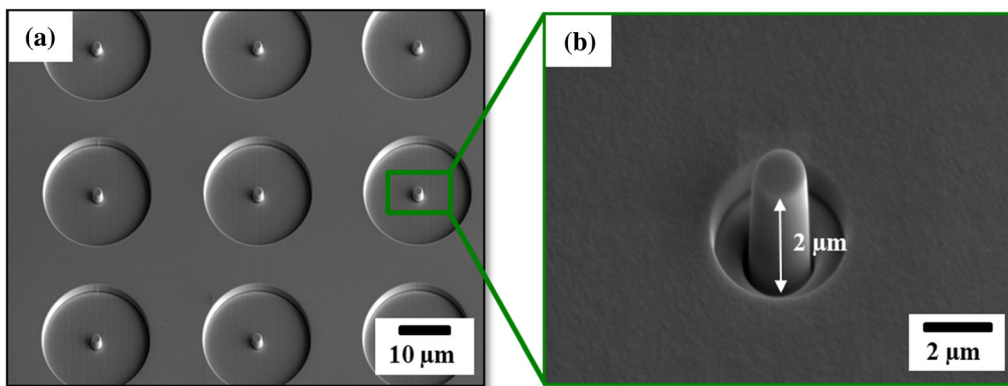

Fig. 1—SEM secondary electron (SE) images of representative micropillars produced by FIB milling in a superalloy thin film. (*a*) An array of nine micropillars after initial manufacturing. (*b*) A high magnification SE-image of a finished micropillar, with a height H ~ 2 μm and width (diameter) W ~ 1.25 μm.
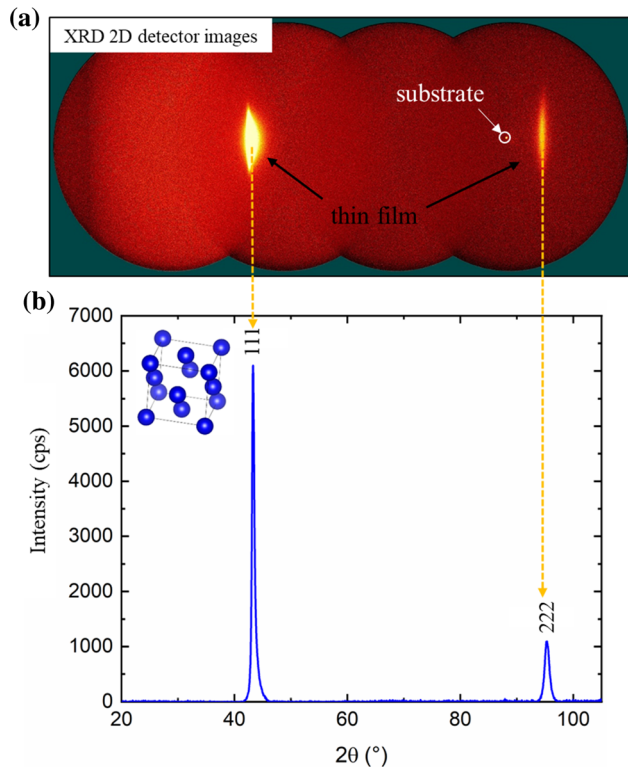
Fig. 2—XRD results obtained from the superalloy thin film showing (*a*) Debye–Scherrer rings, revealing textured structure. The black and white arrows mark the reflections of the thin film and the substrate, respectively. (*b*) A XRD diffraction pattern with two peaks of a FCC crystallographic structure. No secondary phases were detected.

to the film normal. The growth direction of the lamellar grains is highlighted by the white arrow. A grain width of ~ 45 ± 7 nm was measured with Imagic IMS software using the TEM images and linear intercept method.

Furthermore, nanotwins (marked by the red arrows in Figure 4) formed roughly perpendicular to the grain boundaries and growth direction (marked by a white arrow). The twin spacing between two adjacent twins was measured with Imagic IMS software using the linear intercept method and corresponds to ~ 3 ± 1 nm.

B. *Local Micromechanical Properties*

To determine the mechanical properties of the superalloy thin film, nanoindentation and compression tests on micropillars were carried out at RT. Ten nanoindents with a final indentation depth of 100 nm were performed and show a high reproducibility of the results, with a calculated Young's Modulus of 255 ± 6 GPa and a microhardness of 11 ± 0.4 GPa, respectively. Subsequently, compression tests on seven micropillars, with the pillar axis parallel to the lamellar grain boundaries, were performed. Figure 5(a) shows the engineering stress/displacement diagram, with each color representing a different compression test. The engineering stress in MPa was calculated by dividing the applied force of the indenter by the area of the micropillar (height × diameter). For these calculations, the upper diameter of

the micropillar was used. The stress–displacement curves exhibit a linear elastic loading followed by a spontaneous onset of plasticity (exemplarily marked on the blue stress–displacement curve), which is characterized by a sudden deformation event associated with a stress plateau and several displacements bursts. To determine the yield strength, the stress to initiate the first sudden deformation event was evaluated for all seven microcompression experiments and is calculated to be 4.1 ± 0.3 GPa. Representative SEM images of a pillar, corresponding to the blue stress–displacement curve, before and after deformation are displayed in Figure 5(b). The plastic deformation occurs localized at the top of the pillar, showing a shear deformation of the pillar top. All seven micropillars, tested that way, exhibit quite similar deformation patterns with a shear band forming from the top of the pillar and being the primary cause for plastic deformation. Results show a good reproducibility, as indicated by the stress/displacement curves with similar form and critical stress values in Figure 5(a).

C. *Microstructure After Deformation*

After the compression tests, a TEM cross-sectional sample was obtained from the deformed pillar by site-specific FIB milling. This sample corresponds to the stress–displacement curve shown in blue in Figure 5(a). Furthermore, Figure 6(a) shows the TEM bright-field image of the entire deformed pillar, marked by yellow dashed lines, to be distinguished from the outer pillar support applied during lamella preparation. In the top of the pillar, a highly concentrated plastic deformation is visible. This deformation band has a width of around 45 to 85 nm and extends from the pillar surface through the columnar grains and creates a deformation step when leaving the pillar.

In the surrounding of the shear band, lamellar grains with nanotwins can be observed which are in line with the microstructure before deformation, Figures 6(b) through (c). Twin spacing in the vicinity of the deformation shear band is determined to be 3.1 ± 1.0 nm, which is quite similar to the nanotwin width measured prior to deformation. No detwinning or thickening of the twins were observed in the regions close to the shear band. However, the TEM orientation imaging (see Figure 7(a)) revealed that the shear band contains nanocrystalline globular grains with random, very different from the columnar grains, orientations (see color coded orientation information in Figure 7(b)). The structure must have been formed during the deformation process.

IV. DISCUSSION

A. *Microstructure of the As-deposited Thin Film*

The presence of columnar nanograins with a preferred < 111 > orientation of the as-deposited thin films has been frequently reported in the literature for fcc materials.[2,11,28,29] Interestingly, in addition to the
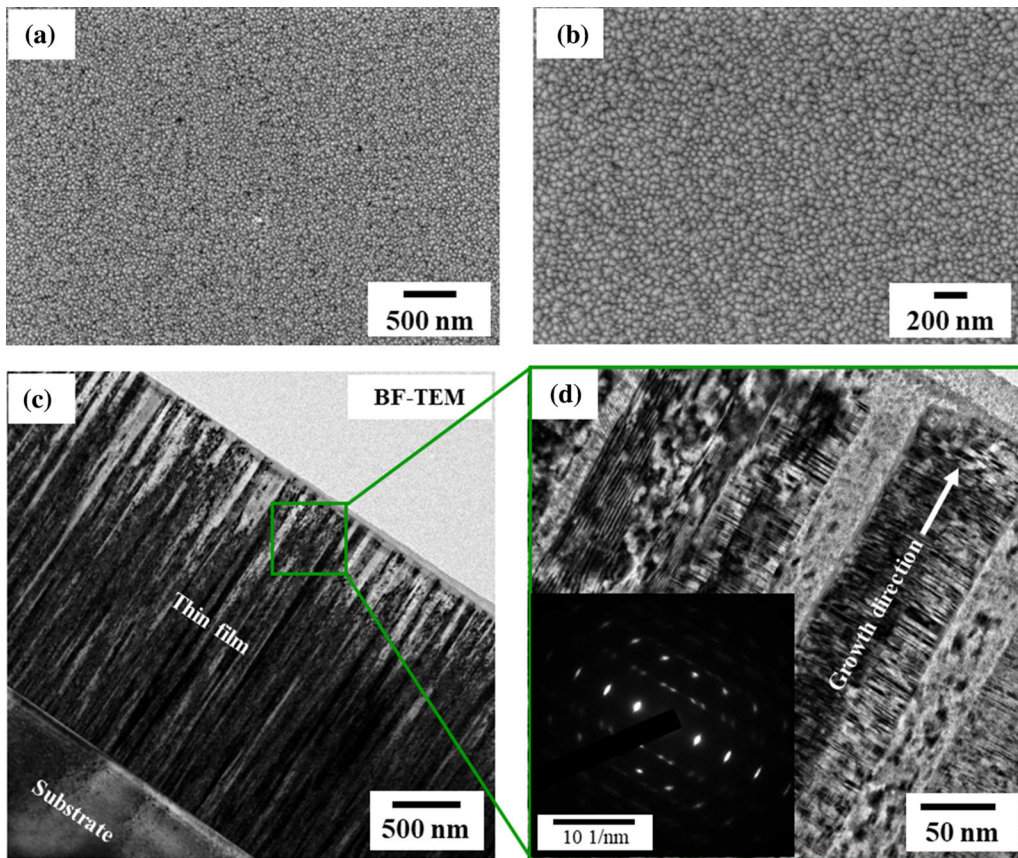
Fig. 3—SE SEM and bright-field (BF) TEM images showing the microstructure of the superalloy thin film: (*a*) and (*b*) SEM surface images of the film with nanograins with a size of ~ 45 ± 7 nm. (*c*) and (*d*) TEM images of a TEM cross-sectional sample, showing the columnar nanograin microstructure of the film and part of the substrate in (c). The grain growth direction is marked by the white arrow in (d). A SAED for pure Ni is included as inset in the lower left corner of the image in (d). Some grains are better visible in the TEM than others due to their crystallographic orientation.

expected nanograined microstructure, densely spaced nanotwins were observed in the present work. The formation of nanotwins is reported to be closely related to the stacking fault energy (SFE) of the alloys[2,11,30,31]: a lower SFE is advantageous for the formability of nanotwins, whereas higher SFE makes the process much more difficult.[31,32] Generally, Ni alloys exhibit relatively high SFEs. However, moderate additions of elements such as Mo and W to the Ni systems, suggested by the calculations performed by Shang *et al.*[33], have been shown to promote the formation of nanotwinned microstructures.[29] Therefore, it is reasonable to assume that the nanotwins in our thin film have formed during deposition. Furthermore, for thin films, sputtering with a very high deposition rate is advantageous for the formation of coherent twin boundaries (CTBs) with high densities.[31,34] Compared to different studies focusing on pure Ni or Ni alloy composition thin films, the columnar nanograins with nanotwins observed in microstructural analyses in our superalloy thin film are in good agreement with the literature data.[2,11,28,29]

Finally, it should be noted that no γ' phase was found in our thin film, only FCC γ phase is present.

B. *Mechanical Properties and Deformation Mechanisms*

The nanoindentation results of the superalloy thin film show a Young's Modulus of around 255 GPa, which is in good agreement with the values of Young's Modulus of ~ 230 GPa[35,36] and ~ 250 GPa[37] reported for bulk SX Ni-based superalloys. Durst *et al.* showed using nanoindentation that there is only a slight difference between the Young's Modulus in γ and γ', with the values for γ being only ~ 5 pct lower. Hardness data and yield strength obtained from nanoindentation and from micropillar testing in our superalloy thin film exhibit very high values both for hardness, of around 11 GPa, and for yield strength, of around 4.1 GPa. According to the literature, there is well-known and widely implemented relationship between hardness H and yield strength σ_y, which is valid for materials exhibiting ideal plastic deformation and no
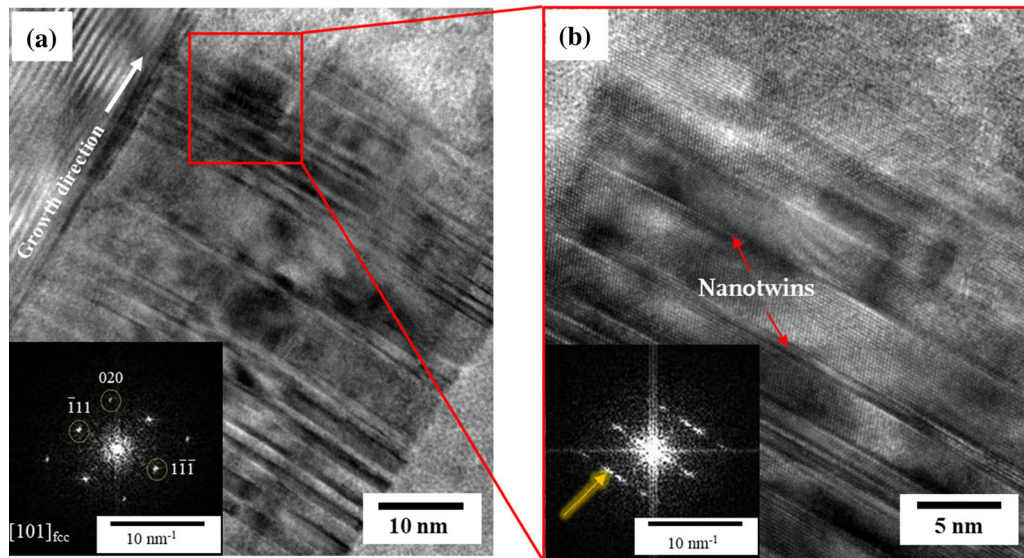
Fig. 4—BF-TEM images highlighting columnar nanograins with nanotwins in the superalloy thin film. (*a*) Representative grain with nanotwins formed almost perpendicular to the grain growth direction (the white arrow). TEM diffraction patterns indicate FCC crystallographic structure with no secondary phases, as shown by the Fast Fourier Transform (FFT) inset in the lower left corner. (*b*) Higher magnification TEM image with visible nanotwins within the nanograin, confirmed by the FFT shown as inset in the lower left corner.

work-hardening.[38–41] This correlation is described by the following equation[38–41]:

$$H = 3 \times \sigma_y. \qquad [1]$$

Independently from identifying the deformation mechanisms during microcompression and nanoindentation in detail, the critical yield stress and hardness of the superalloy thin film are in agreement with the Tabor correlation described in the literature and expressed by Eq. [1].

However, published bulk data of single crystal superalloys, associated with deformation only of the γ matrix, show hardness values of ~ 6.5 GPa for indentation microhardness.[35,37,42] The yield stress results, associated with the deformation of γ and γ', correspond to ~ 1 GPa and were obtained by macro tensile tests.[43,44] In contrast, the critical strength in our superalloy thin film pillars is measured to be 4 GPa, which is almost four times higher than the one occurring in bulk samples. Different studies also investigated critical stresses for the onset of plasticity of CMSX-4 by using circular and rectangle micropillars.[45,46] The measured critical strength for the single crystal superalloys micropillars range between 1.5 and 2 GPa, where generally higher critical strength was observed for smaller pillars. Compared to these rectangular micropillars with similar height and cross-sectional area, the critical stress of the superalloy thin film pillars investigated in this study is still twice as high.

Nanocrystalline materials and alloys, with an average grain size smaller than 100 nm, are reported to exhibit higher strength and hardness then their conventional larger-grained counterparts.[2,47–49] However, these mechanical properties cannot be explained solely by the Hall–Petch relation,[49] which states that with decreasing grain size, the number of dislocations that can pile up at grain boundaries decreases, resulting in increased stresses, necessary for material deformation. The deformation during compression testing in our thin film micropillars occurs through a deformation shear band, starting at the pillar top and running through the lamellar grains (Figure 6). Generally, plastic deformation through shear bands formation is a well-known phenomenon, observed in materials with ultrafine grain sizes (< 300 nm).[49–52] The development of such shear bands is correlated to the decrease of dislocation density of the material due to the nanograined microstructure, resulting in much weaker strain hardening behavior.[49,50,52] Furthermore, the nanograined materials contain a higher grain-boundary volume fraction[48] which plays an important role during deformation. The grain boundaries tend to serve as sources and sinks for dislocations as well as important mechanism for deformation through grain-boundary sliding.[48,49,53]

Additionally, the presence of nanotwins and the spacing between two adjacent twins are critical factors that affect the mechanical properties of the thin film.[2,54,55] Moreover, the thickness of the twins plays an important role in enhancing the strength of the material.[39,49,55] To induce and propagate plastic deformation in the nanotwinned material with very fine, nanometer thick twins, dislocations need to pass across the CTB without the pile-up effect. However, the transmission of single dislocations across CTBs is a complex process, which leads to high critical transmission stress necessary for its completion.[5,31,56] Therefore, nanotwinned materials generally exhibit higher strength than their counterparts without nanotwins. However, below a certain size (in case of nanotwinned Cu below ~ 15 nm[55,57]) the nanotwins tend to have a negative effect during plastic deformation and even
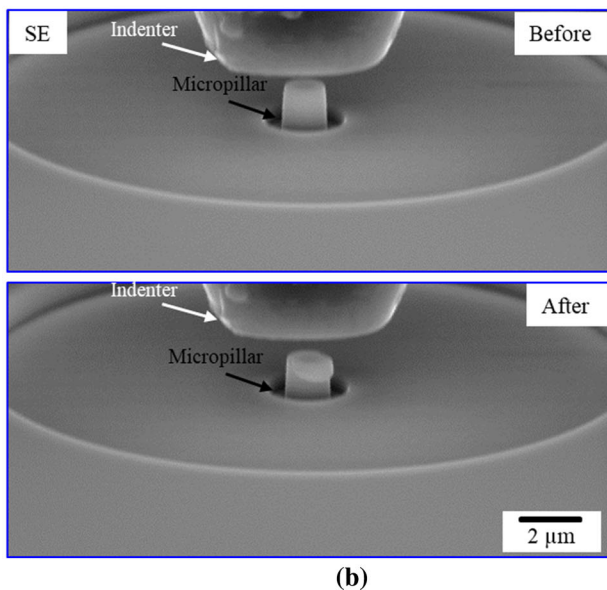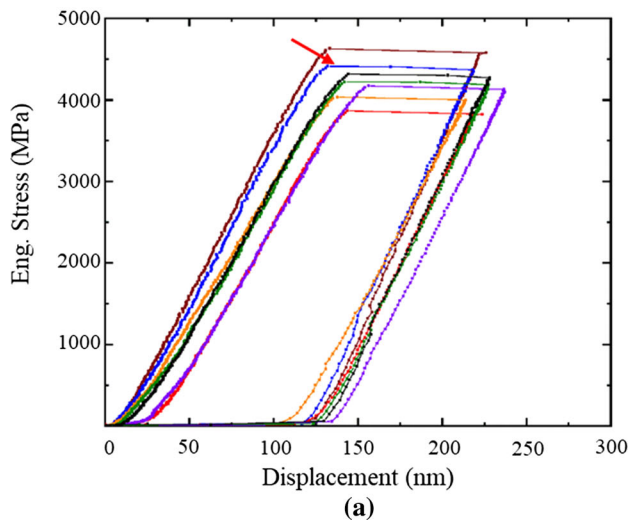
(a)

(b)

Fig. 5—Results from *in-situ* indentation of the micropillars. (*a*) Engineering stress/displacement plot with each colored curve indicating a different pillar test. The red arrow indicates the critical stress for the blue curve. (*b*) Representative SEM images of the pillar, corresponding to the blue curve in (a), prior to and after compression. The micropillar and the indenter are marked with white and black arrows, respectively.

reduce the strength of the alloy through a process, called "detwinning."[31,55,57] However, this softening behavior is reported not to occur in sputtered alloys with CTBs.[31,34,58]

It should also be noted that the nanotwins in the superalloy thin film are aligned perpendicular to the loading direction. As reported in literature[2,59–61] the orientation of the CTBs is crucial for the ongoing deformation mechanism. Jang *et al.*[59] showed that for Cu, CTBs perpendicular to the loading axis deform through dislocation transmission through twin boundaries, while somewhat inclined CBTs are more prone to detwinning. Detwinning was not observed in the superalloy thin film investigated in this study. Although dislocation pile-ups were not observed at the CBTs,
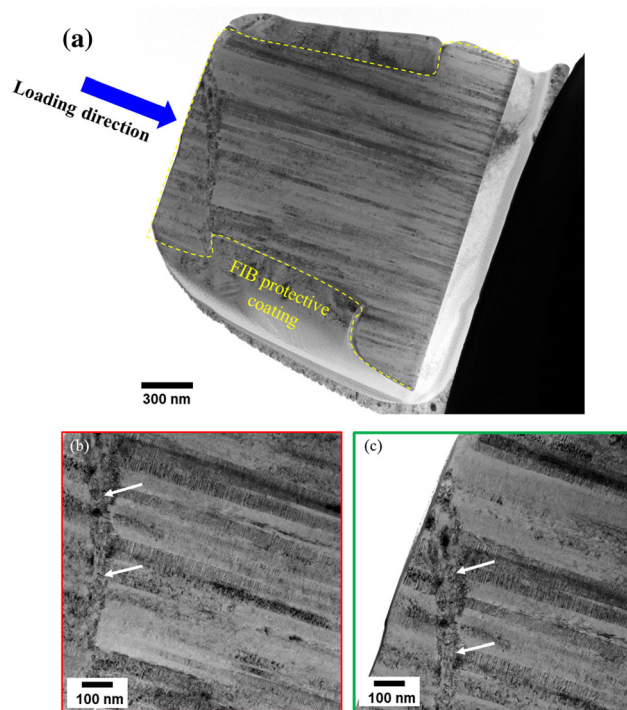

Fig. 6—BF-TEM images of a cross section of the compressed pillar (compare blue stress–strain curve in Fig. 5a). (*a*) Side view of the TEM lamella with the compressed pillar marked by a yellow dashed line. Regions where images with higher magnification were obtained are marked with green and red squares, respectively. (*b*) and (*c*) TEM images with higher magnification along the deformation band of the micropillar, with the white arrow highlighting the shear band.

dislocation transmission between the twins could not be ruled out completely, without high-resolution TEM images of these boundaries. Such images were out of the scope of this study and therefore were not obtained.

In our superalloy thin film, we observe that during compression testing a shear band forms, within which nanocrystalline equiaxed grains have formed (see Figure 7). This seems to happen quickly directly after the first sudden deformation event associated with the initiation of the shear band. Usually, shear band formation shows a multistep process involving detwinning followed by the evolution of detwinned bands into dislocation cells and subsequently the transformation of dislocation cells into globular grains. Finally, the shear band thickens and more nanocrystalline grains form. We could not find any hints for preceding deformation mechanism. The deformation behavior through deformation shear bands with globular grains is very similar to the behavior of Ni–Mo–W thin film pillars studied by Valentino *et al.*[2] In that study, a highly localized deformation in the form of a shear band containing globular grains formed during compression testing. A preceding mechanism such as detwinning could not be found in the publication of Valentino et al. either. Similar to results of Valentino *et al.*[2] the plastic deformation in the superalloy thin film pillars examined in the current study tends to be governed by shear band formation and propagation, without any dislocation gliding, detwinning, or layer bending.
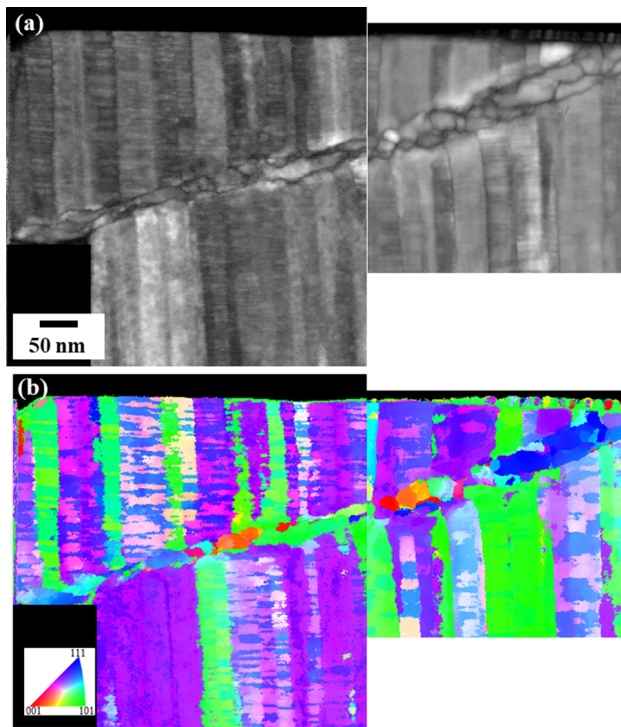
Fig. 7—DigiSTAR Nanomegas TEM orientation images of the deformed pillar, shown in Fig. 6. (*a*) Reconstructed BF images of the shear band in the compressed pillar. (*b*) Inverse pole figure (IPF) map of the region showed in (a).

V. SUMMARY AND CONCLUSION

In-situ compression tests of micropillars produced from a Ni-based superalloy thin film were conducted at RT. The microstructure evolution prior and after the experiments as well as the deformation behavior of the material and the investigation of the local mechanical properties lead to the following conclusions:

(1) Using HiPIMS at 500 °C, a thin film with a ~ 2.5 μm thickness and an almost identical composition to the superalloy ERBO/1 were produced.

(2) The microstructure of the superalloy thin film is characterized by columnar nanograins with a width of ~ 45 ± 7 nm. Inside these grains, fine nanotwins with a thickness of ~ 3 ± 1 nm, were found. They are oriented perpendicular to the film growth direction.

(3) Cylindrical micropillars with the height of ~ 2 μm and a diameter of ~ 1.25 μm were milled in the thin film using a FIB. *In-situ* compression tests exhibit a yield strength of about 4.1 GPa ± 0.3.

(4) Nanoindentation experiments revealed a Young's Modulus for the thin film of 255 ± 6 GPa, which is in good agreement with the previous published SX data. Moreover, the superalloy thin film exhibits a very high microhardness of about 11 GPa.

(5) Plastic deformation of the micropillars occurred through a deformation shear band, starting from the top of the pillar and passing through the

nanotwinned columnar grains. A detailed TEM investigation reveals the formation of globular grains, which formed during the deformation process within the shear band and exhibit random crystallographic orientation. No additional indication of preceding the deformation mechanisms was found. Therefore, further work on the local micromechanical properties of nanotwinned and nanograined Ni-based superalloy thin films should be conducted, to obtain an even better understanding of the deformation processes and their initiation.

COMPETING INTEREST

All authors declare that they have no known competing financial interests or personal relationships that could have appeared to influence the work reported in this paper.

REFERENCES

1. J.A. Krogstad, C. Keimel, and K.J. Hemker: *J. Mater. Res.*, 2014, vol. 29, pp. 1597–608.
2. G.M. Valentino, S. Xiang, L. Ma, K.Y. Xie, M.-R. He, W.C. Oliver, G.M. Pharr, J.A. Krogstad, T.P. Weihs, and K.J. Hemker: *Acta Mater.*, 2021, vol. 204, p. 116507.
3. D.E. Burns, Y. Zhang, T.P. Weihs, and K.J. Hemker: *Thin Solid Films*, 2014, vol. 558, pp. 20–23.
4. C.K. Malek and V. Saile: *Microelectron. J.*, 2004, vol. 35, pp. 131–43.
5. D.E. Burns, Y. Zhang, M. Teutsch, K. Bade, J. Aktaa, and K.J. Hemker: *Scr. Mater.*, 2012, vol. 67, pp. 459–62.
6. R.C. Reed: *The Superalloys: Fundamentals and Applications*, 1st ed. Cambridge University Press, Cambridge, 2006.
7. C. Zhang, K. Feng, Z. Li, F. Lu, J. Huang, Y. Wu, and P.K. Chu: *Acta Mater.*, 2017, vol. 133, pp. 55–67.
8. P. Velvaluri, A. Soor, P. Plucinsky, R.L. de Miranda, R.D. James, and E. Quandt: *Sci. Rep.*, 2021, vol. 11, p. 10988.
9. R. Lima de Miranda, C. Zamponi, and E. Quandt: *Adv. Eng. Mater.*, 2013, vol. 15, pp. 66–69.
10. A.B. Parsa, P. Wollgramm, H. Buck, C. Somsen, A. Kostka, I. Povstugar, P.-P. Choi, D. Raabe, A. Dlouhy, J. Müller, E. Spiecker, K. Demtroder, J. Schreuer, K. Neuking, and G. Eggeler: *Adv. Eng. Mater.*, 2015, vol. 17, pp. 216–30.
11. K. Kim, S. Park, T. Kim, Y. Park, G.-D. Sim, and D. Lee: *J. Alloys Compd.*, 2022, vol. 919, p. 165808.
12. I. Lopez-Galilea, J. Koßmann, A. Kostka, R. Drautz, L. Mujica-Roncery, T. Hammerschmidt, S. Huth, and W. Theisen: *J. Mater. Sci.*, 2016, vol. 51, pp. 2653–64.
13. K. Matuszewski, R. Rettig, H. Matysiak, Z. Peng, I. Povstugar, P. Choi, J. Müller, D. Raabe, E. Spiecker, K.J. Kurzydłowski, and R.F. Singer: *Acta Mater.*, 2015, vol. 95, pp. 274–83.
14. O.M. Horst, D. Adler, P. Git, H. Wang, J. Streitberger, M. Holtkamp, N. Jöns, R.F. Singer, C. Körner, and G. Eggeler: *Mater. Des.*, 2020, vol. 195, p. 108976.
15. G.P. Sabol and R. Stickler: *Phys. Status Solidi (B)*, 1969, vol. 35, pp. 11–52.
16. M. Kateb, H. Hajihoseini, J.T. Gudmundsson, and S. Ingvarsson: *J. Vac. Sci. Technol., A*, 2019, vol. 37, p. 31306.
17. J. Bohlmark, M. Lattemann, J.T. Gudmundsson, A.P. Ehiasarian, Y. Aranda Gonzalvo, N. Brenning, and U. Helmersson: *Thin Solid Films*, 2006, vol. 515, pp. 1522–26.
18. A. Anders: *Surf. Coat. Technol.*, 2014, vol. 257, pp. 308–25.
19. A. Anders: *J. Appl. Phys.*, 2017, vol. 121, p. 171101.
20. H. Zhang, J.-S. Cherng, and Q. Chen: *AIP Adv.*, 2019, vol. 9, p. 35242.
21. W.C. Oliver and G.M. Pharr: *J. Mater. Res.*, 1992, vol. 7, pp. 1564–83.
22. W.C. Oliver and G.M. Pharr: *J. Mater. Res.*, 2004, vol. 19, pp. 3–20.
23. J. Pfetzing-Micklich, S. Brinckmann, S.R. Dey, F. Otto, A. Hartmaier, and G. Eggeler: *Mater.-wiss Werkstofftech*, 2011, vol. 42, pp. 219–23.
24. J.-K. Heyer, S. Brinckmann, J. Pfetzing-Micklich, and G. Eggeler: *Acta Mater.*, 2014, vol. 62, pp. 225–38.
25. H.M. Tawancy: *Oxid. Met.*, 2020, vol. 93, pp. 371–86.
26. A. Basak, S. Holenarasipura Raghu, and S. Das: *J. Mater. Eng. Perform.*, 2017, vol. 26, pp. 5877–84.
27. D. Medlin, K. McCarty, R. Hwang, S. Guthrie, and M. Baskes: *Thin Solid Films*, 1997, vol. 299, pp. 110–14.
28. J.A. Bahena, N.M. Heckman, C.M. Barr, K. Hattar, B.L. Boyce, and A.M. Hodge: *Acta Mater.*, 2020, vol. 195, pp. 132–40.
29. S. Kurz, A. Leineweber, and E.J. Mittemeijer: *J. Mater. Res.*, 2014, vol. 29, pp. 1642–55.
30. X. Feng, J. Zhang, K. Wu, X. Liang, G. Liu, and J. Sun: *Nanoscale*, 2018, vol. 10, pp. 13329–34.
31. I.J. Beyerlein, X. Zhang, and A. Misra: *Annu. Rev. Mater. Res.*, 2014, vol. 44, pp. 329–63.
32. Y. Liu, N. Li, D. Bufford, J.H. Lee, J. Wang, H. Wang, and X. Zhang: *JOM*, 2016, vol. 68, pp. 127–35.
33. S.L. Shang, C.L. Zacherl, H.Z. Fang, Y. Wang, Y. Du, and Z.K. Liu: *J. Phys. Condens. Matter: Inst. Phys. J.*, 2012, vol. 24, p. 505403.
34. X. Zhang and A. Misra: *Scr. Mater.*, 2012, vol. 66, pp. 860–65.
35. M. Göken and M. Kempf: *Acta Mater.*, 1999, vol. 47, pp. 1043–52.
36. K. Demtröder, G. Eggeler, and J. Schreuer: *Mater.-wiss. Werkstofftech*, 2015, vol. 46, pp. 563–76.
37. K. Durst and M. Göken: *Mater. Sci. Eng. A*, 2004, vol. 387–389, pp. 312–16.
38. D. Tabor: *Rev. Phys. Technol.*, 1970, vol. 1, p. 145.
39. L. Lu, R. Schwaiger, Z.W. Shan, M. Dao, K. Lu, and S. Suresh: *Acta Mater.*, 2005, vol. 53, pp. 2169–79.
40. Y.-T. Cheng and C.-M. Cheng: *Mater. Sci. Eng. R. Rep.*, 2004, vol. 44, pp. 91–149.
41. P. Zhang, S.X. Li, and Z.F. Zhang: *Mater. Sci. Eng. A*, 2011, vol. 529, pp. 62–73.
42. S. Neumeier, F. Pyczak, and M. Göken: *Philos. Mag.*, 2011, vol. 91, pp. 4187–99.
43. A. Sengupta, S.K. Putatunda, L. Bartosiewicz, J. Hangas, P.J. Nailos, M. Peputapeck, and F.E. Alberts: *JMEP*, 1994, vol. 3, pp. 73–81.
44. H. Zhang, P. Li, X. Gong, T. Wang, L. Li, Y. Liu, and Q. Wang: *Mater. Sci. Eng. A*, 2020, vol. 782, p. 139105.
45. K. Arora, K. Kishida, and H. Inui: *MRS Proc.*, 2013, vol. 1516, pp. 209–14.
46. K. Arora, K. Kishida, K. Tanaka, and H. Inui: *Acta Mater.*, 2017, vol. 138, pp. 119–30.
47. M. Dao, L. Lu, R. Asaro, J. Dehosson, and E. Ma: *Acta Mater.*, 2007, vol. 55, pp. 4041–65.
48. K. Kumar, H. van Swygenhoven, and S. Suresh: *Acta Mater.*, 2003, vol. 51, pp. 5743–74.
49. M.A. Meyers, A. Mishra, and D.J. Benson: *Prog. Mater. Sci.*, 2006, vol. 51, pp. 427–556.
50. D. Jia, K.T. Ramesh, and E. Ma: *Acta Mater.*, 2003, vol. 51, pp. 3495–509.
51. Q. Wei, D. Jia, K.T. Ramesh, and E. Ma: *Appl. Phys. Lett.*, 2002, vol. 81, pp. 1240–42.
52. Q. Wei, L. Kecskes, T. Jiao, K.T. Hartwig, K.T. Ramesh, and E. Ma: *Acta Mater.*, 2004, vol. 52, pp. 1859–69.
53. H. Hahn, P. Mondal, and K.A. Padmanabhan: *Nanostruct. Mater.*, 1997, vol. 9, pp. 603–06.
54. Z. Wang, C. Wang, Y.-L. Zhao, Y.-C. Hsu, C.-L. Li, J.-J. Kai, C.-T. Liu, and C.-H. Hsueh: *Int. J. Plast.*, 2020, vol. 131, p. 102726.
55. L. Lu, X. Chen, X. Huang, and K. Lu: *Science (New York, N.Y.)*, 2009, vol. 323, pp. 607–10.
56. X. Zhang, A. Misra, H. Wang, M. Nastasi, J.D. Embury, T.E. Mitchell, R.G. Hoagland, and J.P. Hirth: *Appl. Phys. Lett.*, 2004, vol. 84, pp. 1096–98.
57. J. Wang, N. Li, O. Anderoglu, X. Zhang, A. Misra, J.Y. Huang, and J.P. Hirth: *Acta Mater.*, 2010, vol. 58, pp. 2262–70.
58. O. Anderoglu, A. Misra, H. Wang, and X. Zhang: *J. Appl. Phys.*, 2008, vol. 103, p. 94322.
59. D. Jang, X. Li, H. Gao, and J.R. Greer: *Nat. Nanotechnol.*, 2012, vol. 7, pp. 594–601.
60. M. Mieszala, G. Guillonneau, M. Hasegawa, R. Raghavan, J.M. Wheeler, S. Mischler, J. Michler, and L. Philippe: *Nanoscale*, 2016, vol. 8, pp. 15999–6004.
61. Z. You, X. Li, L. Gui, Q. Lu, T. Zhu, H. Gao, and L. Lu: *Acta Mater.*, 2013, vol. 61, pp. 217–27.